ISSN 1330-3651 (Print), ISSN 1848-6339 (Online)
Received: 17 October 2025; Accepted: 16 December 2025

https://doi.org/10.17559/TV-20251017003074
Original scientific paper

Interval-Based Robust Optimisation Scheduling for Integrated Energy Systems Considering Energy Storage Lifespan and Flexible Thermal Load Response

Haoyu MAO

Abstract: The widespread adoption of renewable energy within integrated energy systems introduces significant uncertainty, posing challenges to their stable and economical operation. Mitigating the costly degradation of electrochemical energy storage equipment while effectively managing fluctuations on both the generation and load sides has become a critical issue. Against this backdrop, this paper proposes a scheduling framework integrating interval-type robust optimisation with a two-layer model predictive control approach. During the day-ahead planning phase, an interval-type robust scheduling model is constructed. This model employs *k*-means clustering to partition uncertainty sets for renewable generation and load demand, thereby circumventing the excessive conservatism inherent in traditional robust optimisation. For the intraday phase, a two-layer model predictive control framework is established to smooth the rolling optimisation time scale differences across electricity, heat, gas, and hydrogen loads. Concurrently, a storage lifetime cost term is incorporated into the optimisation objective to extend the energy storage system's lifespan. This is combined with an electricity price-based demand response model to enhance scheduling flexibility. Simulation results demonstrate the proposed method's multifaceted advantages. Compared to conventional robust optimisation, the interval-based robust optimisation model maintains high user satisfaction (96.43%) while reducing average daily system operating costs by approximately 8.24% and lowering the monthly capacity degradation rate of the energy storage system from 1.831% to 1.617%. The intraday robust model predictive control (MPC) demonstrated robust performance under extreme scenarios, with total cost increases of merely 2.91%, significantly lower than the 16.23% observed in conventional MPC. The proposed scheduling strategy, integrating interval robust optimisation with model predictive control, offers an effective solution for addressing robustness, economic efficiency, and equipment lifespan management within integrated energy systems under renewable energy and load uncertainty.

Keywords: demand side response; energy storage device ageing; integrated energy system scheduling; interval-based robust optimisation; model predictive control

1 INTRODUCTION

With the continuous expansion of global energy demand, efficient energy management has become a focal point of research. Integrated energy systems (IES), as an innovative solution for efficiently integrating and managing multiple energy sources, have garnered extensive attention [1]. The growth in energy demand has also exerted significant environmental impacts. Against this backdrop, the development of renewable energy (RE) holds crucial significance for addressing energy crises and environmental pollution [2]. However, the inherent unpredictability of renewable energy poses challenges to the stable operation of power systems. To stabilize the fluctuating power output of renewable generation systems, direct current (DC) microgrids equipped with various energy storage systems (ESS), such as batteries and supercapacitors, have emerged as a popular power generation architecture [3]. In China, the deployment of energy storage equipment is undergoing large-scale promotion. The Chinese government anticipates that by 2027, the country's new energy storage installed capacity will exceed 180 gigawatts [4]. However, high-performance energy storage equipment is costly. During actual operation, as the equipment undergoes repeated charge-discharge cycles, it gradually degrades, posing challenges to the cost of the power system and indeed the entire energy system. Research into the optimisation of energy storage device scheduling has been extensively explored in the literature. For instance, Babazadeh et al. [5] integrated local/global service providers. They comprehensively considered factors such as the charging/discharging characteristics, capacity constraints, and energy losses of energy storage systems. Based on different time scales and actual load demand conditions, they meticulously planned and formulated scientifically sound charging/discharging strategies. Building upon this, they constructed a collaborative energy demand response model. Employing a multi-timescale coordinated control strategy, they rapidly adjusted the output of generation and consumption equipment according to the system's real-time operational status, achieving swift and accurate execution of demand response. Given the model's multiple variables and constraints, these parameters exhibit uncertainty. The method requires computational analysis of each variable during application, thereby reducing the timeliness and effectiveness of demand response. Literature [6] proposed an optimised demand response scheduling (DROS) framework integrating renewable energy sources (RES) with energy storage systems (ESS), yet it did not address enhancing system robustness. This limitation may compromise stable operation under extreme conditions.

Uncertainty during power system operation constitutes a primary factor in grid fluctuations, primarily stemming from two sources: the output variability of renewable energy at the generation end and load fluctuations at the consumer end. Addressing renewable energy output uncertainty, reference [7] defines and calculates the "Admissible Region for Renewable Power Injection (ADMIRE)" to enable quantitative management. Regarding load-side forecasting challenges, reference [8] proposed a multi-timescale dynamic optimal dispatch strategy integrating robust optimisation with MPC-based rolling optimisation. However, this approach excludes energy storage devices and fails to mitigate storage degradation issues during IES operation. Regarding demand fluctuations on the consumer side, numerous studies have introduced electricity price-based demand response to achieve peak shaving and valley filling objectives, yielding notable results. For instance, reference [9] proposes a dynamic pricing (DP) intelligent demand response (DR) model that effectively enhances power system stability and reliability by regulating peak consumption periods. Reference [10] proposes a dynamic energy management framework based on high-precision energy consumption modelling to simulate automated

residential demand response, aiming to quantify consumer energy usage behaviour and accurately estimate the actual quantity of controllable resources. However, none of the aforementioned literature addresses the integration of robust system optimisation with intraday MPC forecasting. This omission not only slightly compromises system stability but also diminishes the model's real-time capability.

Regarding robust optimisation, reference [11] proposes a novel piecewise-distributed robust optimisation method specifically for real-time power dispatch addressing wind forecast error correlations. It develops a piecewise linear decision rule incorporating permissible thresholds for wind forecast errors, enhancing system robustness while delivering high-quality dispatch solutions. Reference [12] constructs a "Feature-Deletion Robust Regression (FDRR) model" based on robust optimisation to address the issue of feature loss during model deployment (at test time) due to network delays, equipment failures, or data attacks, thereby achieving prediction resilience. However, this work does not address integration with intraday prediction models. The model exhibits poor real-time performance and cannot perform MPC rolling optimisation for devices with differing time scales, presenting limitations in engineering forecasting.

Building upon the literature review, the principal contributions of this paper are as follows:

This paper proposes an interval-based robust optimisation model integrating *k*-means clustering with robust scheduling. This approach balances system robustness and economic efficiency, enhancing the adaptability and reliability of the scheduling model to ensure effective IES dispatch.

This paper integrates the interval-based robust optimisation model proposed for the day-ahead stage with rolling MPC for the intraday stage, proposing a two-stage interval-based RO-MPC integrated scheduling model. This model effectively mitigates the issue of inconsistent load time scales during the intraday stage and enhances the robustness of intraday forecasting;

This paper incorporates energy storage devices into the optimisation scope, proposing a scheduling method that optimises the robustness of energy storage equipment. This approach enhances the service life of energy storage devices by optimising intraday depth of charge and discharge (DOD), thereby mitigating the rate of device degradation.

2 SYSTEM MODELLING

2.1 IES Construction

Utilising advanced technologies such as renewable energy (RE), power-to-gas (P2G) units, gas turbines (GT), electrolysis devices (ED), and other conversion equipment (CE), various energy flows, including electricity, heat, and gas, undergo transformation [13]. Concurrently, with time- or power-flexible thermal loads, the system regulates thermal demand via gas storage tanks while employing electrochemical storage to modulate electrical load, enabling bidirectional demand response. Electrochemical storage primarily utilises lithium-ion batteries, supplemented by fuel cells for electricity storage to meet both short- and long-term energy requirements [14]. The comprehensive energy system model is as Figure 1:

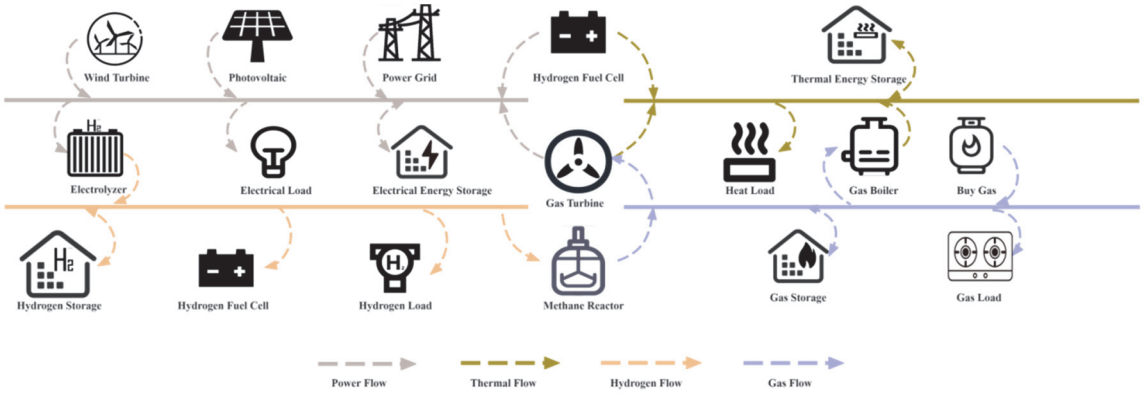

Figure 1 IES architecture diagram

2.2 Modelling of Energy Storage Systems

Energy storage systems constitute a vital component of IES. Batteries can flexibly store and release energy to balance fluctuations, coordinating generation at the source side with consumption at the user side [15]. Simultaneously, they guide load adjustments through electricity price signals or coordinate with heat pumps to regulate thermal loads. This reduces load fluctuations and curtailment rates for wind and solar power within IES, ensuring their flexibility. The fundamental mathematical model for electrochemical energy storage is

$$E_i^t = \left(1-\xi_i\right)E_i^{t-\Delta t} + \left(\vec{P}_i\vec{\eta}_i - \frac{\vec{P}_i}{\vec{\eta}_i}\right)\Delta t\,.$$

In the equation, E_i^t denote the energy stored in the *i*-th electrochemical energy storage device during the operational time t; ξ_i represents the energy loss rate of the electrochemical energy storage system; $\vec{P}_i$ and $\vec{P}_i$ denote the charging and discharging power of the electrochemical energy storage system respectively; $\vec{\eta}_i$ and $\vec{\eta}_i$ denote the charging and discharging efficiency of the system respectively; Δt denotes the time interval.

Within IES, electrochemical energy storage can make charging and discharging decisions based on the imbalance power caused by discrepancies between renewable energy generation and load demand. The imbalance power ΔP_t is calculated as follows:

$$\Delta P_t = P_{\Sigma}^t - P_L^t \tag{1}$$

where P_{Σ}^t denotes the total output of all power generation equipment within the IES; P_L^t represents the electrical load power of all equipment within the IES.

When $\Delta P_t < 0$, this indicates P_{Σ}^t fails to meet load demand, prompting the electrochemical energy storage system to discharge. If $\left|\Delta P_t\right| > \vec{P}_i$, the electrochemical energy storage discharges at rated power. Upon reaching minimum capacity, the remaining unmet electricity demand constitutes the load deficit $\vec{P}_L^t$, calculated as:

$$\vec{P}_L^t = P_L^t - P_{\Sigma}^t - \vec{P}_i \tag{2}$$

$$\psi_L^t = \frac{\sum_{t=1}^{T} \vec{P}_L^t}{\sum_{t=1}^{T} P_L^t} \tag{3}$$

where ψ_L^t denotes the load deficit rate at time t.

Within IES, load fluctuations induce frequent charge-discharge cycles in energy storage systems, thereby accelerating their lifespan degradation. This degradation correlates with the number of charge-discharge cycles (N_{cycle}) and the DOD. The cycle count and DOD for an energy storage system under varying load conditions can be calculated using the cycle count method. Assuming the initial capacity of the energy storage system is C_0 and the capacity after n charge-discharge cycles is C_n, the capacity decay rate η_1 can be expressed as:

$$\eta_1 = 1 - \frac{C_n}{C_0} \tag{4}$$

where, η_1, N_{cycle}, and DOD are related as follows:

$$\eta_1 = a N_{\text{cycle}}^b \text{DOD}^c \tag{5}$$

where a, b, and c are constants specific to the battery type. If the rated power of the electrochemical energy storage system is a constant P_{rated}, its DOD can be expressed as:

$$\text{DOD} = \frac{\int_{t_1}^{t_2} \left|P(t)\right| \mathrm{d}t}{C_0 P_{\text{rated}}} \tag{6}$$

where $P(t)$ denotes the charge/discharge power of the electrochemical energy storage system at time t, t_1 and t_2 represent the time intervals for charging and discharging, respectively.

2.3 Demand Response Analysis

For IES encompass both electrical and thermal loads, with thermal energy utilisation exhibiting characteristic time delays and thermal inertia. Consequently, thermal loads also participate in demand response. In such cases, electrochemical energy storage systems within the IES are primarily utilised for electrical-thermal regulation, achieving complementary energy exchange between electricity and heat [17].

2.3.1 Electric Load Flexibility in Demand Response

If, within the IES, the electricity load at time t_1 prior to demand response is denoted as $\tilde{P}_{t_1}^a$, and the electricity price at time t_2 prior to response is denoted as $c_{t_2}^a$, then the formula for calculating electricity load demand elasticity is:

$$\chi_{t_1, t_2} = \frac{\Delta \tilde{P}_{t_1}}{\tilde{P}_{t_1}^a} \cdot \frac{c_{t_2}^a}{\Delta c_{t_2}} \tag{7}$$

where: $\Delta \tilde{P}_{t_1}$ represents the change in electricity load at time t_1 following demand response; Δc_{t_2} represents the change in electricity price at time t_2; χ_{t_1, t_2} represents the elasticity coefficient.

The formula for calculating the change in electricity load after incorporating the load elasticity coefficient into price-demand response (PDR) is:

$$\begin{bmatrix} \frac{\Delta P_1}{\tilde{P}_1^a} & \frac{\Delta P_2}{\tilde{P}_2^a} & \cdots & \frac{\Delta P_t}{\tilde{P}_t^a} \end{bmatrix}^T = \begin{bmatrix} \chi_{11} & \chi_{12} & \cdots & \chi_{1\mathrm{T}} \\ \chi_{21} & \chi_{22} & \cdots & \chi_{2\mathrm{T}} \\ \vdots & \vdots & \cdots & \vdots \\ \chi_{t1} & \chi_{t2} & \cdots & \chi_{\mathrm{TT}} \end{bmatrix} \begin{bmatrix} \frac{\Delta c_1}{c_1^a} & \frac{\Delta c_2}{c_2^a} & \cdots & \frac{\Delta c_t}{c_t^a} \end{bmatrix}^T \tag{8}$$

Within the IES, electrical load primarily comprises two types: fixed load and transferable load. Thus, the formula for calculating the demand response-adjusted electrical load quantity P_L^t at time t is:

$$P_L^t = \hat{P}_L^t + \breve{P}_L^t = \tilde{P}_t^a \chi_t \left(1 + \frac{\Delta P_t}{\tilde{P}_t^a}\right) \tag{9}$$

$$\begin{cases} 0 < \breve{P}_L^t \le \breve{P}_L^{\max} \\ \sum_{t=1}^{T} \breve{P}_L^t \Delta t = \Delta \tilde{P}_{\Sigma} \end{cases} \tag{10}$$

where: $\hat{P}_L^t$ and $\breve{P}_L^t$ denote the fixed electrical load and transferable electrical load within the IES at time t, respectively; $\breve{P}_L^{\max}$ represents the maximum variable electrical load power; $\Delta \tilde{P}_{\Sigma}$ denotes the total capacity of variable electrical loads.

2.3.2 Thermal Load Flexibility in Demand Response

Within IES, thermal energy on the demand side

exhibits characteristic time delays and thermal inertia during transmission. To ensure effective demand response, thermal load scheduling is incorporated. The formula for calculating thermal load P_r is:

$$P_r(t)=\frac{A\omega(W_1-W_2)}{\Delta t} \tag{11}$$

where: Adenotes the heated area of the thermal load; ω represents the heat dissipation coefficient; W_1 and W_2 denote indoor and outdoor temperatures respectively.

Within IES, thermal load primarily consumes energy through temperature variations and can be categorised into transferable thermal load $\left(\hat{P}_r\right)$ and fixed thermal load $\left(\overline{P}_r\right)$. Within comfort zones, users exhibit low sensitivity to temperature changes, resulting in thermal load exhibiting fuzziness and delay characteristics. It must be ensured that this remains within a defined range:

$$\begin{cases}\overline{P}_{\mathrm{r}}^{\max}=\dfrac{A\omega\left(\hat{W}_{\max}-W_0\right)}{\Delta t}\\ \overline{P}_r^{\min}=\dfrac{A\omega\left(\hat{W}_{\min}-W_0\right)}{\Delta t}\\ \hat{P}_r^{\max}=\dfrac{\left(\tilde{W}_{\max}-W_0\right)}{\Delta t}\\ \hat{P}_r^{\min}=\dfrac{\left(\tilde{W}_{\min}-W_0\right)}{\Delta t}\end{cases} \tag{12}$$

A thermal load elastic response model analogous to electrical load is established as:

$$\begin{bmatrix}\dfrac{\Delta P_{r,1}}{P_{r,1}^0} & \dfrac{\Delta P_{r,2}}{P_{r,2}^0} & \cdots & \dfrac{\Delta P_{r,T}}{P_{r,T}^0}\end{bmatrix}^T=\begin{bmatrix}\kappa_{11} & \kappa_{12} & \cdots & \kappa_{1T}\\ \kappa_{21} & \kappa_{22} & \cdots & \kappa_{2T}\\ \vdots & \vdots & \ddots & \vdots\\ \kappa_{T1} & \kappa_{T2} & \cdots & \kappa_{TT}\end{bmatrix}\begin{bmatrix}\dfrac{s_1}{s_{\mathrm{ref}}^1} & \dfrac{s_2}{s_{\mathrm{ref}}^2} & \cdots & \dfrac{s_T}{s_{\mathrm{ref}}^T}\end{bmatrix}^T \tag{13}$$

where: $\overline{P}_r^{\max}$ and $\overline{P}_r^{\min}$ denote the maximum and minimum power of fixed thermal load; $\vec{W}_0$ and $\vec{W}_0$ represent thermal input and output temperatures; $\hat{W}_{\max}$ $\tilde{W}_{\max}$and $\hat{W}_{\min}$ denote the upper and lower temperature limits of fixed thermal load; $\hat{P}_r^{\max}$ and $\hat{P}_r^{\min}$ denote the maximum and minimum power of transferable thermal load; $\tilde{W}_{\max}$ and $\tilde{W}_{\min}$ denote the upper and lower temperature limits of transferable thermal load; $\kappa_{i,j}$ denotes the thermal load elasticity coefficient; s_t denotes the temperature regulation signal at time t; s_{ref}^t denotes the reference value of the temperature regulation signal at time t.

Electricity demand elasticity is deeply coupled with the economic dispatch depth of electrochemical energy storage, thereby reducing grid pressure during peak periods. Thermal load elasticity, leveraging temperature control's physical characteristics, synergises with the multi-energy conversion capabilities of energy storage [18], enhancing the system's adaptability to renewable energy fluctuations.

3 DAY-AHEAD ROBUST DISPATCH MODEL

3.1 Objective Function of the RO Dispatch Model

Electrical and thermal load flexibility provides flexibility for demand response, but uncertainties in wind and solar output and load demand may affect scheduling effectiveness. To ensure a balance between economic efficiency and reliability [19], an electrochemical energy storage demand response dispatch model for IES must be developed. This model incorporates electrical and thermal load elasticity while integrating the regulation capabilities of electrochemical energy storage systems [20]. It includes electrical and thermal load elasticity coefficients and energy storage constraints within the dispatch framework. The objective function for this model is:

$$\min_{x,y}\max_{z}\min_{W_{\mathrm{sys}}}F(x,y,z) \tag{14}$$

$$\begin{aligned}F=&\sum_{t=1}^{T}\left(c_1\bar{V}_t^g\cdot\Delta t\right)+\sum_{t=1}^{T}\left(\bar{c}^a\bar{P}_{\mathrm{grid},t}^k\right)\Delta t+\\ &+\sum_{t=1}^{T}\sum_{n=1}^{N}\left(c_2P_{\Sigma}^t\cdot\Delta t\right)-\sum_{t=1}^{T}c_3\left(P_{\mathrm{ele}}^*(t)-\tilde{P}_t^a\right)\Delta t-\\ &-\sum_{t=1}^{T}c_4\left(P_r^*(t)-P_{r,t}^0\right)\Delta t+\sum_{t=1}^{T}c_5\left(q_t^g-q_{t-1}^g\right)+\\ &+\sum_{t=1}^{T}c_6\eta_1\end{aligned} \tag{15}$$

In the equation: x denotes the dispatch continuous variable, encompassing the output power of generating units and fuel cells; y denotes a variable ranging from 0 to 1, encompassing the start/stop status of generating units and the charging/discharging power and capacity of electrochemical energy storage systems; z denotes the random variable; c_1 denotes the natural gas price; $\bar{V}_t^{\mathrm{g}}$ denotes the natural gas input rate of the CCHP unit within the IES; $\bar{c}^a$ and $\bar{c}^{\mathrm{a}}$ denote the electricity purchase and sale prices from the grid, respectively; c_3 represents the benefit coefficient of transferable power load demand response in the IES; $P_{\mathrm{ele}}^*(t)$ and $P_r^*(t)$ denote the electricity and thermal load at time t following demand response, respectively; c_4 represents the benefit coefficient for transferable thermal load demand response within the IES; c_5 indicates the equipment start-stop cost coefficient within the IES; q_t^g and q_{t-1}^g denote the equipment start-stop status at times and , respectively; c_6 signifies the energy storage device degradation cost coefficient.

3.2 Construction of Interval-Type Uncertainty Sets

Based on historical values, the output is divided into n_w intervals using the k-means method. The standard deviation, mean, variance, and quantiles are calculated for each interval. Uncertainty sets are then constructed for

each interval using the *k*-means formula:

$$\min J = \sum_{i=1}^{n_w} \sum_{x \in C_i} x - \mu_i^2 \tag{16}$$

where, C_i denotes the *i*-th cluster; μ_i represents the cluster centre; and n_w is determined using the elbow method.

Employing the above method, the number of intervals and their division points for the interval-type uncertain set can be determined: μ_i represents the discontinuity points of the interval division.

Uncertainty set of this model is:

$$W_K^i = \begin{Bmatrix} P_K^i(t) \mid \mu_K^i(t) - \\ -z_{a/2}^{i,w} \sigma_K^i(t) \le P_K^i(t) < \mu_K^i(t) + \\ + + z_{a/2}^{i,K} \sigma_K^i(t), \forall t \end{Bmatrix} \tag{17}$$

where: *K* represents wind power, photovoltaic output and electrical load; W_K^i denote the uncertainty sets for wind power, photovoltaic output, and load respectively within interval i; $z_{a/2}^{i,K}$ represent the upper $a/2$ quantiles of uncertainty for wind power, photovoltaic output, and load respectively within interval *i*; $\sigma_K^i(t)$ denote the standard deviations for wind power, photovoltaic output, and load respectively; $\mu_K^i(t)$ denote the means for wind power, photovoltaic output, and load respectively. The load uncertainty set encompasses four load types: electricity, heating, gas, and hydrogen.

The final uncertainty set takes the following form:

$$W_{\text{sys}} = W_K \tag{18}$$

3.3 Constraints

Upon completing the objective function design for the robust scheduling model of electrochemical energy storage demand response in IES, corresponding constraints must be established to ensure the completeness of the robust optimisation model, as detailed below:

(1) Energy Balance Constraint

The electricity balance constraint is the core condition ensuring real-time supply-demand equilibrium within the system. In robust scheduling, this constraint must encompass the worst-case scenario of renewable energy output [21], guaranteeing that the IES maintains supply-demand balance under any fluctuations. The formula for this constraint is:

$$P_{\Sigma}^t + \vec{P}_{\text{grid},t}^k + \sum_{i=1}^{n_{\text{es}}} \vec{P}_i^t = P_{\text{L}}^t + \sum_{i=1}^{n_{\text{es}}} \vec{P}_i^t + \vec{P}_{\text{grid},t}^k \tag{19}$$

$$P_L^t = \hat{P}_L^t + \breve{P}_L^t \tag{20}$$

where: $\vec{P}_{\text{grid},t}^k$ and $\vec{P}_{\text{grid},t}^k$ denote the electrical power purchased from and sold to the grid by the system at time *t*, respectively.

(2) Thermal Energy Balance Constraint

The thermal energy balance constraint adjusts the thermal load curve through transferable or reducible thermal loads, thereby enhancing system flexibility. The constraint condition is expressed as:

$$P_r(t) = \bar{P}_r(t) + \hat{P}_r(t) = P_r^{\Sigma} \tag{21}$$

where: P_r^{Σ} represents the total thermal power generated.

(3) Electrochemical Energy Storage State Constraints

Electrochemical energy storage systems are pivotal to achieving optimal robust demand response scheduling within IES. Therefore, constraints must be imposed on the charging and discharging states of electrochemical energy storage systems, calculated as follows:

$$\begin{cases} 0 < \vec{\mathrm{P}}_i \le \bar{\mathrm{P}}_i^{\max} \\ 0 < \vec{P}_i \le \vec{P}_i^{\max} \end{cases} \tag{22}$$

(4) Electrochemical Energy Storage Device Lifespan Degradation Constraint

To safeguard the operational lifespan of electrochemical energy storage equipment, a lifespan degradation constraint must be established. This constraint is expressed as follows:

$$\eta_1 \le \eta_1^{\max} \tag{23}$$

In the equation, $\eta_1^{\max}$ denotes the permissible maximum attenuation rate.

(5) Load power shortage rate constraint:

During demand response operations within the IES, the energy storage system discharges to meet load demand, potentially causing load power shortage rates. To ensure uninterrupted supply to users, the load power shortage rate must remain below the maximum permissible value $\psi_{L,\max}^t$ (set at $\psi_{L,\max}^t = 10\% \cdot P_{\text{L}}^t$):

$$\psi_L^t < \psi_{L,\max}^t \tag{24}$$

Designing according to the aforementioned constraints and solving this model yields the final robust dispatch results.

3.4 Model Solution

Traditional optimisation algorithms struggle to directly solve robust scheduling models due to their uncertain sets and complex constraints. Therefore, duality theory and the Column and Constraint Generation (C&CG) algorithm can be employed for solution.

For the uncertain components within the robust scheduling model, dual theory can be employed to transform them into deterministic equivalent forms. Taking the electrical power balance constraint as an example, refining the constraint as follows:

$$P_w(t)+P_{pv}(t)+P_{\mathrm{GT}}(t)+P_{\mathrm{FC}}(t)+\sum_{i=1}^{n_{\mathrm{es}}}\vec{P}_i^t = P_L^t+\sum_{i=1}^{n_{\mathrm{es}}}\overleftarrow{P}_i^t+P_{\mathrm{P2G}}(t),\ \forall z \tag{25}$$

where $P_{\mathrm{GT}}(t)$ denotes gas turbine output; $P_{\mathrm{FC}}(t)$ represents fuel cell output power; and $P_{\mathrm{P2G}}(t)$ indicates the total gas output power from all electro-to-gas conversion equipment within the system.

Let the uncertainty term be $a(z,t)=P_w(t)-P_L^t+P_{pv}(t)$ and the remaining variables be the deterministic terms denoted as $b(x, y, t)$. Then the original constraints simplify to:

$$a(z,t)+b(x,y,t)\le 0,\ \forall z\in W_{\mathrm{sys}} \tag{26}$$

By strong duality theory, the above constraint is equivalent to $(x,y,t)\le -\max_{z\in W_{\mathrm{sys}}} a(z,t)$, transforming the problem into solving $\max_{z\in W_{\mathrm{sys}}} a(z,t)$. Combining the boundary of the uncertainty set:

$$\begin{aligned}\max_{z\in W_{\mathrm{sys}}} a(z,t) &= \max_{P_w\in\left[P_w^-,P_w^+\right]} P_w(t)+\\ &+\max_{P_{pv}\in\left[P_{pv}^-,P_{pv}^+\right]} P_{pv}(t)-\min_{P_{\mathrm{ele}}\in\left[P_L^{t-},P_L^{t+}\right]} P_L^t(t)=P_w^+(t)+\\ &+P_{pv}^+(t)-P_L^{t-}(t)\end{aligned} \tag{27}$$

Substituting this into the original constraints yields the following determinacy constraints:

$$\begin{aligned}&P_{\mathrm{GT}}(t)+P_{\mathrm{FC}}(t)+\sum_{i=1}^{n_{\mathrm{es}}}\vec{P}_i^t-\sum_{i=1}^{n_{\mathrm{es}}}\overleftarrow{P}_i^t-\\ &-P_{\mathrm{P2G}}(t)\le-\left[P_w^+(t)+P_{pv}^+(t)-P_L^{t-}\right],\ \forall t\end{aligned} \tag{28}$$

where, for variable Y, Y^- and Y^+ represent the upper and lower bounds of variable Y within the corresponding uncertainty set interval.

The remaining constraints are solved similarly. This method converts all uncertain constraints into deterministic constraints. After conversion to deterministic constraints, the problem is divided into a main problem (MP) and subproblems (SP):

(1) MP

Solve x^* and y^* to minimise the total cost F across a given set of worst-case cases. At each iteration, the new worst-case scenario identified by the subproblem is incorporated into the main problem as a constraint, rendering the main problem solution robust against the discovered worst-case cases.

(2) SP

After solving the main problem, the solutions x^* and y^* are obtained. Within the uncertainty set, the worst-case uncertain parameters are then identified, i.e., those that maximise the system cost.

The specific workflow is illustrated in Figure 2.

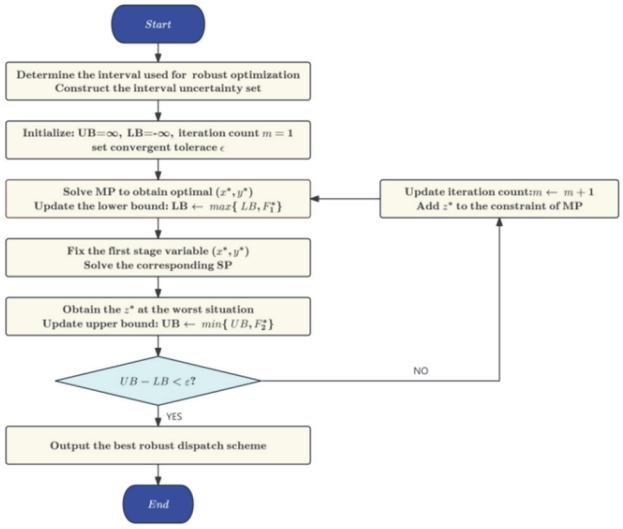

Figure 2 Flowchart of interval-based RO solution

4 INTRADAY TWO-LAYER MPC FORECASTING MODEL

4.1 Construction of Upper and Lower Models

As previously noted, due to users' relatively low sensitivity to temperature variations, thermal load exhibits a time-lagged response. In stark contrast, electricity demand demonstrates extremely high sensitivity to thermal load, with pronounced temporal variability and a significantly shorter time scale than thermal load. Consequently, when performing intraday MPC forecasting, it is necessary to mitigate this mismatch in temporal scales. To this end, this paper proposes a dual-layer MPC forecasting model to mitigate the temporal scale disparity between electricity and thermal loads.

(1) Upper Layer Model

The upper layer model encompasses thermal and gas loads, both exhibiting longer variation cycles. Consequently, the upper layer model employs a 24-hour prediction time horizon and a 1-hour control time horizon.

The state variable matrix for this layer is:

$$\boldsymbol{x}_{\mathrm{up}}=\begin{bmatrix}E_{\mathrm{ther}}(k),\ G_{\mathrm{demand}}(k),\ \mathrm{SOC}(k),\\ P_{H_2,\mathrm{load}}^{\mathrm{pred}}(k),\ P_L^{\mathrm{pred}}(k),\ s_k\end{bmatrix} \tag{29}$$

where $E_{\mathrm{ther}}(k)$, $G_{\mathrm{demand}}(k)$, $\mathrm{SOC}(k)$, $P_{H_2,\mathrm{load}}^{\mathrm{pred}}(k)$ and $P_L^{\mathrm{pred}}(k)$ represent thermal storage state, gas load demand, electrochemical storage SOC, hydrogen load, and estimated electricity load, respectively.

The corresponding control variable matrix is:

$$U=\left[P_{\mathrm{heat}}^{\mathrm{set}}(k),\ G^{\mathrm{set}}(k),\ P_{\mathrm{ESS}}(k),\ \Delta s_k\right] \tag{30}$$

where, $P_{\mathrm{heat}}^{\mathrm{set}}(k)$, $G^{\mathrm{set}}(k)$ and $P_{\mathrm{ESS}}(k)$ denote the thermal power setpoint, gas load setpoint, and storage power of electrical storage device at time k, respectively.

The thermal load prediction equation is:

$$P_{\text{ther}}^{\text{pred}}(k+1)=\alpha_{\text{ther}}\cdot P_{\text{ther}}^{\text{pred}}(k)+ \\ +(1-\alpha_{\text{ther}})\cdot P_{\text{ther}}^{\text{meas}}(k)+\beta_{\text{ther}}\cdot(T_{\text{out}}(k)-T_{\text{set}}(k)) \tag{31}$$

where, $P_{\text{therl}}^{\text{pred}}(k)$ denotes the thermal load forecast at time k; $P_{\text{ther}}^{\text{meas}}(k)$ represents the historical mean thermal load at time k; $T_{\text{out}}(k)$ indicates the ambient temperature at time k; $T_{\text{set}}(k)$ signifies the set temperature at time k; α_{ther} and β_{ther} are constant coefficients determined by historical empirical values.

The air load prediction equation is:

$$G_{\text{demand}}^{\text{pred}}(k+1)=\gamma_{\text{gas}}\cdot G_{\text{demand}}^{\text{pred}}(k)+ \\ +(1-\gamma_{\text{gas}})\cdot G_{\text{demand}}^{\text{meas}}(k)+\delta_{\text{gas}}.P_{\text{CHP}}^{\text{sche}}(k) \tag{32}$$

In the equation, $G_{\text{demand}}^{\text{pred}}(k)$ denotes the predicted air load at time k; $G_{\text{demand}}^{\text{meas}}(k)$ represents the historical mean at time k; $P_{\text{CHP}}^{\text{sche}}(k)$ indicates the output power of the CHP unit at time k; γ_{gas} and δ_{gas} are both constant coefficients determined by historical empirical values.

The objective function for the upper-layer MPC is:

$$\min\sum_{k=1}^{24}\begin{bmatrix} c_{\text{heat}}P_r(k)+c_{\text{gas}}G(k)+ \\ +\beta\cdot J_{\text{aging}}^{\text{upper}}(k)+\lambda_{\text{thermal}}\cdot \\ \cdot\left(P_{\text{thermal}}(k)-P_{\text{thermal}}^{\text{pred}}(k)\right)^2+ \\ +\lambda_{\text{gas}}\cdot\left(\text{G}_{\text{gas}}(k)-G_{\text{gas}}^{\text{pred}}(k)\right)^2 \end{bmatrix} \tag{33}$$

where the lifetime decay penalty term is:

$$J_{\text{aging}}^{\text{upper}}(k)=a\left(\frac{\left|P_{\text{ESS}}(k)-P_{\text{ESS}}(k-\Delta k)\right|}{P_{\text{rated}}}\right)^b \\ \left(\text{DOD}_{\text{pred}}(k)\right)^c \tag{34}$$

(2) Lower-layer model

The lower layer model primarily serves the refined control of electrochemical energy storage and accommodates rapid fluctuations in electrical load. Furthermore, as electrolytic hydrogen production units can respond swiftly (within minutes) to electricity prices or power commands, their load is rapidly adjustable. This fundamentally differs from the slow dynamic characteristics of thermal loads, hence hydrogen load should also reside within the lower layer model. To ensure timeliness, the prediction time horizon is set to 4 hours and the control time horizon to 15 minutes.

The state space of the lower layer model x_{low} is:

$$x_{\text{low}}=\begin{bmatrix}\text{SOC}(k),\text{DOD}(k),N_{\text{cycle}}(k),\text{Temp}(k), \\ P_{\text{load}}^{\text{pred}}(k),P_{\text{load}}(k),\text{SOC}_{H_2}(k),P_{H_2,\text{load}}^{\text{pred}}(k)\end{bmatrix} \tag{35}$$

where, $\text{SOC}(k)$, $\text{DOD}(k)$, $N_{\text{cycle}}(k)$ and $\text{Temp}(k)$ denote the state of charge (SOC), DOD, equivalent cycle count, and battery temperature at time t respectively. $P_{\text{load}}^{\text{pred}}(k)$ and $P_{\text{load}}(k)$ represent the predicted and actual values of the electrical load respectively.

The hydrogen load prediction model is:

$$P_{H_2,\text{load}}^{\text{pred}}(k+1)=\alpha_{H_2}P_{H_2,\text{load}}^{\text{pred}}(k)+ \\ \left(1-\alpha_{H_2}\right)P_{H_2,\text{load}}^{\text{meas}}(k)+\beta_{H_2}\cdot\Delta P_{\text{produce}}(k) \tag{36}$$

where, $P_{H_2,\text{load}}^{\text{pred}}(k)$ denotes the predicted hydrogen load at time k; $P_{H_2,\text{load}}^{\text{meas}}(k)$ represents the historical average hydrogen load at time k; and $\Delta P_{\text{produce}}(k)$ indicates the hydrogen power generated at time k.

The forecast model for the electricity load is:

$$P_L^{\text{pred}}(k+1)=\alpha_s P_L^{\text{pred}}(k)+ \\ (1-\alpha_s)P_L^{\text{meas}}(k)+w_L(k)+\Delta P_L^{\text{pred}}(k) \tag{37}$$

$$\Delta P_L^{\text{pred}}(k+1)=\beta_s\left|P_L^{\text{meas}}(k)-P_L^{\text{pred}}(k)\right|+ \\ +(1-\beta_s)\Delta P_L^{\text{pred}}(k) \tag{38}$$

where, $P_L^{\text{meas}}(k)$ denotes the historical mean of the power load at time k; α_s and β_s denote smoothing coefficients; $w_L(k)$ denotes the load prediction uncertainty, with $w_L(k) \in W_{\text{sys}}$; $\Delta P_L^{\text{pred}}(k)$ denotes the difference between the predicted and actual values.

Based on this, the objective function integrating electricity load and lifetime perception is established as:

$$\min\sum_{j=1}^{15}\begin{bmatrix}\alpha_1\left(P_{\text{grid}}(j)-P_{\text{grid}}^{\text{ref}}(j)\right)+ \\ +\alpha_2\left(P_{\text{ESS}}(j)-P_{\text{ESS}}^{\text{ref}}(j)\right)+ \\ +\alpha_3\cdot J_{\text{aging}}^{\text{lower}}(j)+\alpha_4\left(P_{\text{L}}(j)-P_{\text{L}}^{\text{pred}}(\text{j})\right)+ \\ +\alpha_5\left(\text{P}_{H_2}(j)-P_{H_2,\text{load}}^{\text{pred}}(\text{j})\right)\end{bmatrix} \tag{39}$$

where the lifetime cost function is expressed as:

$$J_{\text{aging}}^{\text{lower}}(j)=a\cdot\left(\frac{\left|P_{\text{ESS}}(j)\right|}{\text{P}_{\text{rated}}}\right)^b\cdot\left(\text{DOD}_{\text{pred}}(j)\right)^c \tag{40}$$

4.2 Constraints

(1) Real-time cycle count constraint:

$$N_{\text{cycles}}(k+1)=N_{\text{cycles}}(k)+\frac{\int_{tk}^{t_{k+1}}\left|P_{\text{ESS}}(t)\right|\text{d}t}{2\cdot C_0\cdot\text{DOD}(k)} \tag{41}$$

(2) Capacity degradation constraint:

$$\eta_1(k) \le \eta_1^{\max} \tag{42}$$

(3) SOC health window constraint:

$$\mathrm{SOC}_{\min} + \delta \le \mathrm{SOC}(k) \le \mathrm{SOC}_{\max} - \delta \tag{43}$$

where δ donates the safety margin, preventing extreme SOC from exerting excessive impact on battery lifespan.

(4) State transition equation:

$$\mathrm{SOC}(k+1) = \mathrm{SOC}(k) + \frac{\bar{\eta}_i P_{\mathrm{ESS}}^{\mathrm{ref}}(k)\Delta t - \frac{P_{\mathrm{ESS}}^{\mathrm{ref}}(k)\Delta t}{\vec{\eta}_i}}{C_0} \tag{44}$$

4.3 Intraday Interval-Based RO-MPC Model

During the intraday phase, model robustness must still be ensured. This necessitates basing MPC predictions upon the results of the day-ahead interval-based RO. The objective function for the intraday interval-based RO is:

$$\min_{u} \max_{w \in W_{\mathrm{sys}}} J(x, u, w) \tag{45}$$

$$\text{s.t.} \begin{cases} x^*(k+1) = f\left(x^*(k), u(k), w(k)\right) \\ \eta_1(k) \le \eta_1^{\max}, \forall k \\ \mathrm{SOC}_{\min} \le \mathrm{SOC}(k) \le \mathrm{SOC}_{\max} \\ u_{\min} \le u(k) \le u_{\max} \\ \Delta P_{\mathrm{imbalance}}(k) = P_{\mathrm{load}}^{\mathrm{pred}}(k) - P_{\mathrm{load}}(k) \end{cases} \tag{46}$$

During the intraday phase, the interval segmentation points for the intraday phase are determined using a *k*-means method based on intraday parameters. Based on this interval, the DRO problem for the intraday phase is addressed.

Following completion of the above optimisation, MPC will proceed based on these results. To ensure predictive model validity, the intraday interval-based RO-MPC adopts a 1-hour prediction time horizon and a 15-minute control time horizon.

4.4 Model Solution

As the solution process for the interval-based RO model has been outlined previously, this section focuses solely on the dual-layer MPC model's solution workflow. The specific solution flowchart is depicted below:

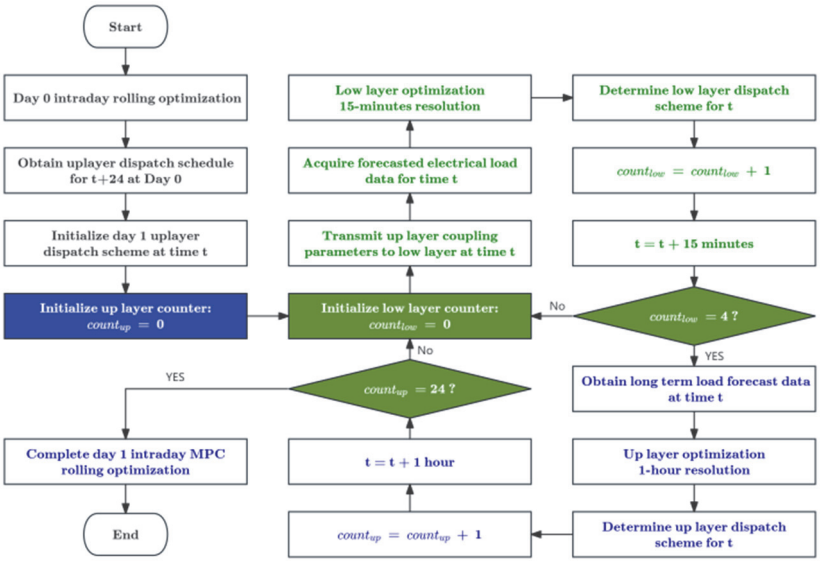

Figure 3 Flowchart of the two-layer MPC solution algorithm

5 CASE STUDY

5.1 Parameter Configuration

To validate the effectiveness of the proposed method within IES, simulations were conducted using an industrial park IES as a case study. The optimisation model was implemented in MATLAB-R2023b using the YALMIP toolbox, with solutions obtained via the GUROBI-11.0.3 solver. All simulations were executed on a computer with identical configurations. The parameters of the IES are presented in Table 1 while the electricity purchase and sale price are detailed in Table 2.

Table 1 IES parameters

Parameter	Value	Unit
C_0	2500	kWh
P_{rated}	800	kW
$\eta_1^{\max}$	2%	/
ω	1.5	W/(m²·°C)
c_1	3.0	¥/m³
c_2	0.1	¥/kWh
c_3	0.1	¥/kWh
c_4	0.1	¥/kWh
c_5	400	¥/time
c_6	400	¥/%
$\bar{\eta}_i$	0.85	/
$\vec{\eta}_i$	0.75	/
Wind turbine maintenance cost	0.05	¥/kWh
Photovoltaic maintenance cost	0.05	¥/kWh
GB and GT maintenance cost	0.04	(¥ / kWh)
P2G equipment maintenance cost	0.045	(¥ / kW)

Table 2 Time-of-use electricity purchase and dale tariffs

Time period	Electricity purchasing price	Electricity selling price
Peak (16:00-22:00)	1.067 ¥/kWh	0.318 ¥/kWh
Valley (00:00-06:00)	0.425 ¥/kWh	
Norm (6:00-16:00; 22:00-24:00)	0.746 ¥/kWh	

5.2 Determination of the Coefficient for the Upper and Lower Layer Model Lifespan Cost

The coefficient for the lifetime cost term must be determined through simulation experiments. Therefore, during simulation, the relevant coefficient was varied between [0, 1] in increments of 0.02 to analyse the total cost of the MPC objective function. The coefficient corresponding to the minimum total cost was selected. The simulation results are presented in Fig. 4.

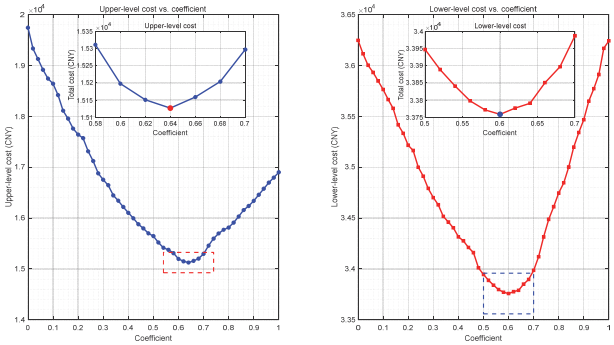

Figure 4 Total cost of upper and lower layer models under different coefficients

Based on the results in Fig. 4, it can be concluded that when $\beta = 0.64$ and $\alpha_3 = 0.6$, the objective function achieves its minimum value. Therefore, this value is adopted as the coefficient for the lifetime cost.

5.3 Model Validity Analysis

5.3.1 Construction of User Satisfaction Degree

To further validate the scheduling effectiveness of the proposed method, a satisfaction index for electrical and thermal loads is employed as an evaluation metric. This index measures the satisfaction level of loads following scheduling and is as follows:

$$\begin{cases} \ell_{\mathrm{a}} = 1 - \dfrac{\tilde{P}^{a}_{t,\mathrm{d}}}{\tilde{P}^{a}_{t,0}} \\ \ell_{\mathrm{r}} = 1 - \dfrac{P^{\mathrm{r}}_{t,\mathrm{d}}}{P^{\mathrm{r}}_{t,0}} \end{cases} \tag{47}$$

where $\tilde{P}^{a}_{t,0}$, $P^{r}_{t,0}$, $\tilde{P}^{a}_{t,d}$ and $P^{r}_{t,d}$ denote the initial electrical and thermal loads interrupted electrical and thermal loads respectively; ℓ_a and ℓ_r denote the electrical, thermal load satisfaction degree respectively.

5.3.2 Generation of Extreme Cases

To conduct interval-based RO effectiveness analysis under extreme conditions, this paper introduces 20% random fluctuations to the acquired IES data to simulate extreme cases. All random fluctuations follow a uniform distribution on the interval [−1, 1] with a coefficient equal to the historical mean. Elements potentially exhibiting significant variability include: wind power, photovoltaic output, and the loads. To comprehensively evaluate the role of robust optimisation, this study generates 30 daily-level extreme cases and hourly-level extreme cases within a single day.

5.3.3 Analysis of the Effectiveness of the Day-Ahead Robust Scheduling Model

During the day-ahead period, the model employed herein is an interval-based robust dispatch model. To demonstrate the efficacy of the proposed interval-based robust dispatch model, this section presents a comparative analysis using the following case studies:

Case 1: Under conventional conditions, employing traditional robust scheduling combined with MPC;

Case 2: Under normal circumstances, employing interval-based robust scheduling combined with MPC.

Prior to conducting the effectiveness analysis, the interval division points and number of intervals were determined through a combination of *k*-means clustering and the elbow method, serving as the foundation for the interval-based RO. Following the establishment of the interval-based RO intervals, simulations were conducted for the total cost, user satisfaction, and energy storage device ageing status (1-capacity decay rate) over a one-month period, alongside the SOC and DOD of energy storage devices within a day. These results were then analysed and compared.

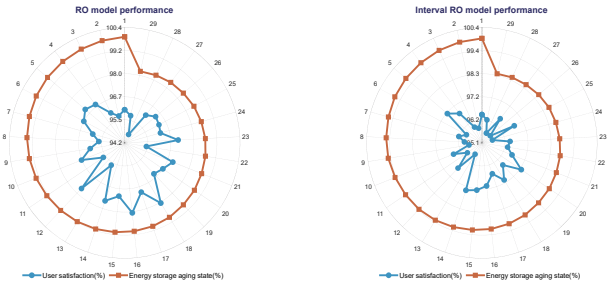

Figure 5 User satisfaction and equipment ageing under traditional RO v.s. interval-based RO models

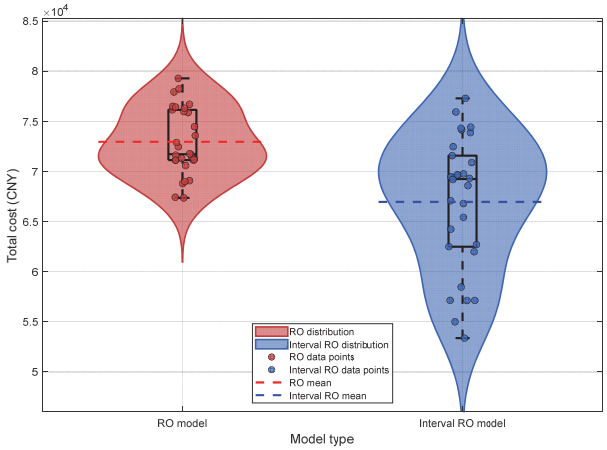

Figure 6 Comparison of total system costs between conventional RO and interval-based RO systems

Table 3 Day-ahead parameters for conventional RO and interval RO models

Model	Average cost / ¥	Average degree of satisfaction	Capacity decay rate
RO	72.96×10^3	96.41%	1.831%
Interval RO	66.95×10^3	96.43%	1.617%

Figure 5 illustrates user satisfaction and the degradation state of energy storage equipment over one month under different robust optimisation methods, while Fig. 6 presents the comparison of total system operating costs. It is evident that employing traditional robust optimisation versus the proposed interval-based robust optimisation method during the day-ahead scheduling phase significantly impacts both the degradation rate of energy storage equipment and user satisfaction. Specifically, the traditional RO model yields a capacity degradation rate of 1.831% for the energy storage system. In contrast, the interval-based robust optimisation model, employing k-means clustering, achieves a capacity degradation rate of 1.617% after one month of operation, making a reduction of 0.214%. Concurrently, this approach ensures exceptionally high user satisfaction. This improvement stems from the interval-based RO method's avoidance of universally extreme conservative strategies. Instead, it implements robust optimisation within specific intervals, thereby maintaining overall system robustness while mitigating accelerated ageing of energy storage equipment caused by excessive conservatism.

Regarding total operating costs, the interval-based RO method also demonstrated significant advantages. Results indicate that the average daily operating cost decreased from 72960 ¥ under traditional RO to 66950 ¥, representing a reduction of approximately 8.24%. This demonstrates that interval-based RO can effectively lower system operating costs and extend the service life of energy storage equipment while maintaining user satisfaction and system robustness. Furthermore, examining cost distribution reveals that costs under traditional RO are relatively concentrated, whereas those under interval-based RO are more dispersed. This phenomenon stems from the traditional RO's globally conservative strategy, which generates excessive redundant robustness costs, thereby diminishing the inherent variability in necessary system costs. In contrast, the interval-based RO adjusts its optimisation strategy according to the characteristics of each interval, eliminating non-essential robustness costs. This narrows the system's operational costs to theoretical necessity, causing a more dispersed distribution.

Furthermore, the average DOD under the traditional RO model is 13.75%, whereas the interval-based RO achieves 9.17%. The larger single DOD of traditional RO further increases its cycle count. According to the aforementioned lifespan degradation model, interval-based RO exhibits lower values for both DOD and cycle count compared to traditional RO. This contributes to delaying capacity degradation in energy storage devices and extending their operational lifespan. This constitutes the principle by which interval-based RO enhances the lifespan of energy storage equipment.

5.3.4 Intraday Interval-Based RO-MPC Scheduling Model Effectiveness Analysis

The intraday phase employs a two-layer interval-based RO-MPC model, enhancing system prediction accuracy while ensuring robustness. To demonstrate this model's efficacy, the following case studies are analysed comparatively:

Case 1: Under normal conditions, employing a traditional MPC scheduling model

Case 2: Under normal conditions, employing the proposed interval-based RO-MPC scheduling model

Case 3: Under extreme conditions, employing the conventional MPC scheduling model

Case 4: Under extreme conditions, employing the proposed interval-based RO-MPC scheduling model

For the four cases above, a comparative analysis is conducted on the total cost, user satisfaction, energy storage device degradation status, and daily SOC and DOD for each day within a month under conventional conditions; For the 30 cases under extreme conditions, comparative analysis is conducted on total cost, customer satisfaction (note: although extreme case data is generated based on actual conditions, extreme cases are logically discrete, i.e., non-continuous on a temporal scale, thus precluding the derivation of equipment ageing status under extreme conditions), daily SOC of energy storage equipment, and DOD. Concurrently, MPC prediction outcomes and average computational processing times for all models under both cases are calculated.

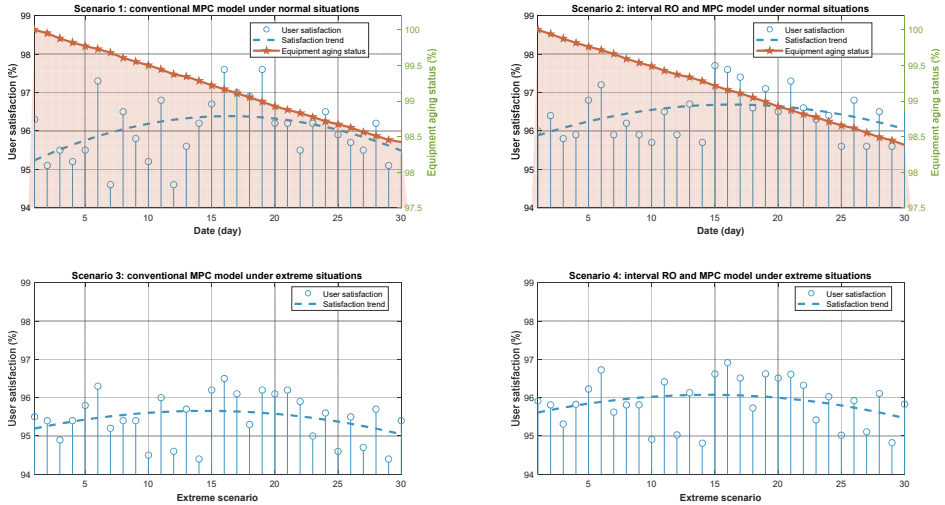

Figure 7 User satisfaction and energy storage device ageing over one month across four cases

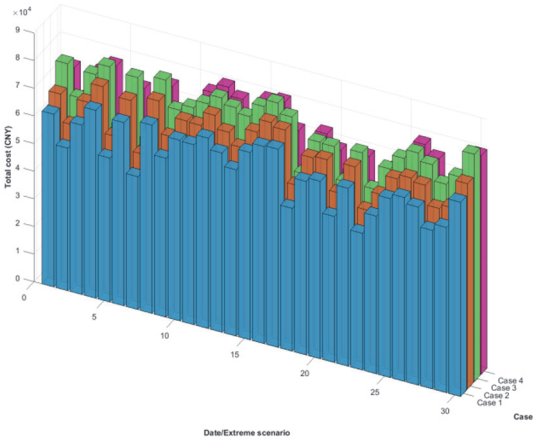

Figure 8 System total cost under four cases

Table 4 Average user satisfaction and average total cost across four cases

Case	User satisfaction degree	Total cost / ¥
1	96.017%	61856.2
2	96.427%	66952.0
3	95.063%	71892.9
4	95.883%	68899.0

Table 5 Energy storage device ageing status and average DOD

Case	1	2	3	4
Ageing status	1.58%	1.62%	\	\
DOD	7.917%	9.167%	11.167%	10.625%

Figure 7 illustrates the daily user satisfaction levels across four cases alongside the monthly degradation state of energy storage equipment under normal conditions. As evident from Figure 7, user satisfaction under conventional conditions generally follows a pattern of being "high in the middle and low at both ends". This trend is primarily driven by three factors: Firstly, insufficient model data at the initial stage. This stems mainly from inadequate data available for model optimisation during the initial phase, resulting in a certain degree of model bias; Secondly, during the middle period, as the model gains sufficient training data, its accuracy improves. Concurrently, the device's condition remains relatively sound, leading to a corresponding rise in user satisfaction. Thirdly, towards the end of the month, accelerated device ageing impairs the model's predictive precision, resulting in reduced accuracy and consequently lower user satisfaction. In contrast, user satisfaction trends in extreme cases appear more gradual. This is because extreme case data lacks temporal continuity, representing merely aggregated results from discrete instances.

Table 4 presents the mean values for user satisfaction and total cost across the four cases. The data indicates that compared to Case 1, Case 2 employs a more conservative decision-making approach by incorporating interval-type RO, resulting in a slight increase in user satisfaction (approximately 0.430%). However, to achieve this heightened conservatism, the system's total cost rises by 5059.8 ¥, representing an increase of approximately 8.24%. Concurrently, the increased reliance on energy storage devices to achieve a more conservative decision-making approach slightly elevated the DOD for these devices compared to Case 1. Consequently, the equipment degradation rate in Case 2 also rose marginally (approximately 0.04%).

However, then optimisation cost of interval-based RO model decreased by 2993.9 ¥ compared to non-interval-based RO under extreme conditions, representing a 4.16% reduction. When comparing Case 1 to Case 3 and Case 2 to Case 4 respectively, the traditional MPC optimisation model saw its cost increase by 10036.7 ¥ under extreme conditions, an approximate rise of 16.23%, while user satisfaction decreased by 0.954%. In contrast, the proposed interval-based RO-MPC model exhibits a total cost increase of merely 1974 ¥, representing an approximate 2.91% rise, with user satisfaction declining by 0.544%. From a total cost perspective, employing the interval-based RO-MPC reduces the percentage increase in total cost under extreme conditions by 13.32%. Regarding user satisfaction, the percentage decline is mitigated by 0.4%. Consequently, the interval-based RO-MPC enhances the system's robustness, enabling it to better address fluctuations under extreme conditions.

Figure 8 further illustrates the distribution of total system costs across the four cases. It is evident that total costs in extreme cases exhibit a significant increase compared to their corresponding conventional counterparts. In conventional situation, the interval-based RO incurs a certain robustness cost due to its inherent conservatism, resulting in slightly higher costs than non-robust methods. However, this cost trade-off yields superior performance maintenance under extreme conditions, significantly narrowing the cost increase. This demonstrates the interval-based RO's distinct advantage in enhancing system operational stability.

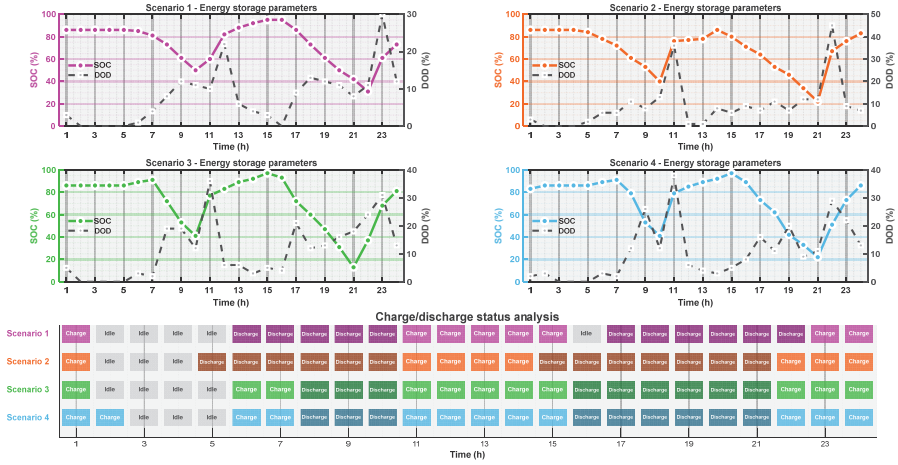

Figure 9 Status of energy storage equipment within a day

During the intraday phase, Figure 9 illustrates relevant parameters of the energy storage device's state. It is evident that during peak periods, all four models can promptly release stored energy to meet demand. Conversely, during off-peak periods, the models opt to charge the energy storage device, thereby achieving the system's peak shaving and valley filling objectives.

As illustrated by Figure 9, the SOC and DOD exhibit inverse fluctuations throughout the day, with each segment of the curve corresponding to specific supply-demand relationships and dispatch strategies at particular times. The SOC increase segments primarily occur during the morning, afternoon, and late night periods. In the morning and afternoon segments, due to higher renewable energy generation (wind and solar), particularly before 16:00, the model decides to charge the energy storage devices to alleviate grid load. Conversely, the SOC decline segments occur during morning and evening peak consumption periods. As user demand increases while renewable generation is relatively low during these times, energy storage systems release stored power to maintain grid stability. The night-time SOC increase stems from substantially reduced user consumption over time, resulting in excess generation exceeding demand. The model consistently directs charging to energy storage systems to absorb surplus electricity, thereby elevating SOC levels.

Integrating data from Figure 9 and

Table **5** reveals that under conventional conditions, the conservative nature of interval-based RO results in a somewhat higher DOD for energy storage systems compared to MPC-only approaches. However, during extreme cases, the pure MPC framework causes a 3.25% increase in DOD. In contrast, the model employing interval-based RO combined with MPC scheduling exhibits only a 1.458% rise in DOD. This significantly reduced increase in DOD demonstrates the model's improvement in enhancing energy storage systems' resilience to extreme conditions.

Table 6 Computer processing duration v.s. model time scale

Model	Interval RO	Upper layer	Lower layer
Average solving time / seconds	63.091	1.122	1.783
Time scale	24 hours	1h	15 min

To better reflect the magnitude of MPC prediction errors, the Table 7 presents the Mean Relative Error (MRE) for each load under various cases:

Table 7 Ratio of the mean load forecast error to the mean load for each load

Case	Electrical load	Thermal load	Gas load	Hydrogen load	Average error
1	3.85%	3.42%	4.10%	3.71%	3.77%
2	5.45%	5.31%	5.73%	6.08%	5.64%
3	8.16%	7.94%	8.05%	8.50%	8.16%
4	7.00%	7.20%	6.10%	7.44%	6.94%

Table 8 Prediction errors of upper and lower layer mpc models

Case	Average error of upper layer model	Average error of low layer model	Difference value (low layer - up layer)
1	3.76%	3.78%	0.02%
2	5.52%	5.77%	0.25%
3	8.00%	8.33%	0.33%
4	6.65%	7.22%	0.57%

Figure 10 illustrate the relationship between the rolling values and reference values of the upper and lower layer MPC models, calculating their Mean Absolute Error (MAE). The figures demonstrate that the MPC prediction model proposed herein accurately reflects the temporal trends of various loads. Combined with the MRE presented in Table 7, it is evident that this MPC prediction model not only precisely captures trends but also exhibits high predictive accuracy. Under conventional conditions (Case 1 and 2), the mean relative errors for the four load types predicted by this MPC model were 3.77% and 5.39% respectively, both representing minimal deviations. The slightly higher error in Case 2 primarily stems from the conservative nature of interval-based RO. This conservatism causes the MPC to prioritise robustness against extreme cases during forecasting, sacrificing some predictive accuracy to maintain robustness, resulting in a marginal decrease in forecast precision. However, this trade-off proves worthwhile. Comparing Case 3 and 4 reveals that under conditions of significant load and renewable energy output fluctuations, without employing the proposed interval-based RO-MPC model, the MRE for the four loads increases by 4.31%, 4.52%, 3.95%, and 4.79% respectively compared to conventional MPC optimisation. with the average MRE for the four loads increasing by approximately 4.39%. In Case 4, employing the proposed interval-based RO-MPC model resulted in MRE increases of 1.55%, 1.89%, 0.37%, and 1.36% for the four loads respectively. The average MRE increase was merely 1.29%. Comparing the interval-based RO-MPC model with the standard MPC model, the MRE improvement decreased by 4.1%, fully demonstrating the effectiveness of the proposed interval-based RO-MPC model in enhancing the robustness of MPC forecasting models.

The data in indicates that the computational processing speed of the proposed model is significantly lower than the engineering timescale of the actual cases. This demonstrates that the model possesses strong real-time capabilities and can be effectively applied in practical engineering contexts.

Furthermore, data from Table 7 indicates that the upper-layer MPC models exhibit smaller errors than the lower-layer models. Combined with data from

Table 8, the relative prediction error of the lower-layer models slightly increases compared to the upper-layer models across all cases. This stems from the algorithmic principles of the two-layer MPC model presented herein: the lower-layer MPC model operates upon the upper-layer model, meaning errors in the upper layer are directly propagated to the lower layer, resulting in generally larger errors in the lower model. Furthermore, the lower model operates on a finer temporal scale, making it more susceptible to random fluctuations that significantly impact its predictions, thus yielding greater relative errors compared to the upper model.

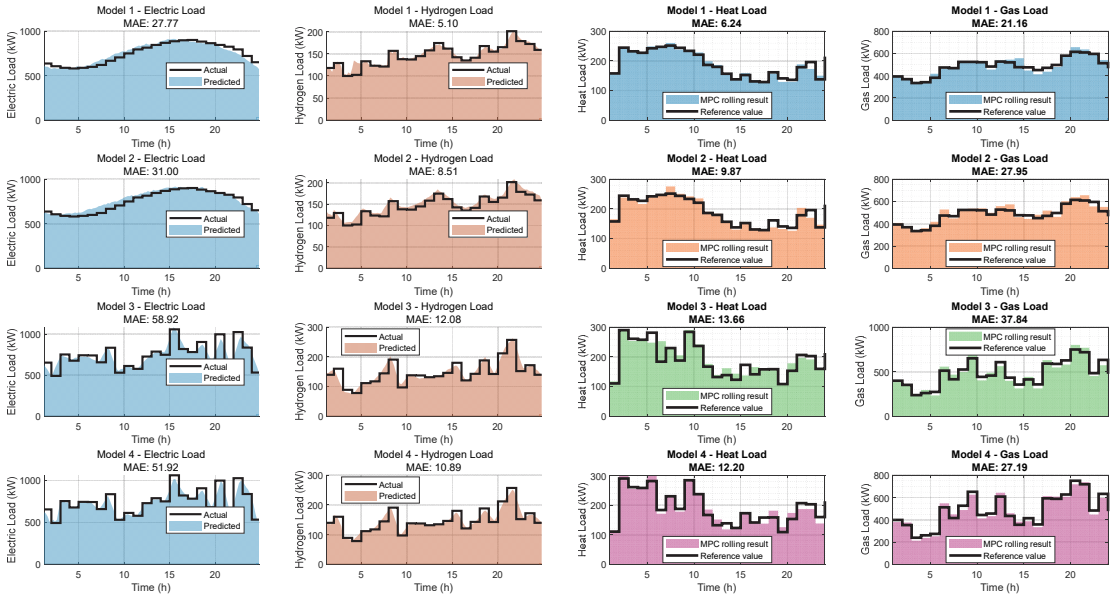

Figure 10 Comparison of lower layer (left two columns) and upper layer (right two columns) rolling results with reference values

7 CONCLUSION

This paper proposes an innovative scheduling framework integrating interval-based robust optimisation (RO) with two-layer model predictive control (MPC) for integrated energy systems. Its primary contribution is a novel methodological synergy that effectively balances robustness, economy, and equipment lifespan.

The key innovation is the interval-based RO using *k*-means clustering to partition uncertainty sets, which strategically mitigates the excessive conservatism of traditional RO. Case results demonstrate its dual advantage: maintaining high user satisfaction while reducing daily operating costs by 8.24% and lowering the monthly storage capacity degradation rate from 1.831% to 1.617%.

For intraday scheduling, the two-layer MPC framework is another significant innovation, resolving the temporal scale mismatch between different energy loads. Crucially, embedding the day-ahead interval RO into rolling MPC creates a robust rolling horizon strategy. Under extreme scenarios, this integrated approach limits cost increases to merely 2.91%, far outperforming conventional MPC (16.23%), proving its superior resilience.

Furthermore, explicitly incorporating a storage lifetime degradation model into the optimisation represents a critical advancement for sustainable IES operation. The framework proactively optimises depth of discharge, extending equipment service life.

In summary, this work presents a practical and holistic paradigm that co-optimises operational economics, uncertainty resilience, and capital asset longevity, offering a significant reference for managing future renewable-integrated energy systems.

8 REFERENCES

[1] Zhang, L., He, Y., Wu, H., & Hatziargyriou, N. D. (2025). An optimal scheduling framework for integrated energy systems using deep reinforcement learning and deep learning prediction models. *IEEE Transactions on Smart Grid. Advance online publication*, *16*(6), 4620-4634. https://doi.org/10.1109/TSG.2025.3599511

[2] Shi, Z., Wang, W., Huang, Y., Li, P., & Dong, L. (2022). Simultaneous optimisation of renewable energy and energy storage capacity with hierarchical control. *CSEE Journal of Power and Energy Systems*, *8*(1), 95-104. https://doi.org/10.17775/CSEEJPES.2019.01470

[3] Liu, S., Dong, G., Ying, Y., Lai, C.-M., & Mishima, T. (2025). Asymmetrical duty-cycle limit control-based multiport bidirectional DC-DC converter for distributed energy storage system applications. *IEEE Transactions on Power Electronics*, *40*(7), 9518-9542. https://doi.org/10.1109/TPEL.2025.3540557

[4] National Development and Reform Commission. (2025). *Special action plan for the large-scale construction of new-type energy storage (2025-2027)*.

[5] Babazadeh, V., Shayeghi, H., Jalili-Irani, A., & Aghajani, G. (2025). Optimal demand response in virtual power plant using local/global service providers in interaction with energy storage systems. *Journal of Cleaner Production*, *496*, 145058. https://doi.org/10.1016/j.jclepro.2025.145058

[6] Ramesh, B., Khedkar, M., Kotha, S. K. et al. (2025). A demand response-based optimal scheduling framework considering renewable sources and energy storage: A deterministic approach. *Electrical Engineering*, *107*, 1885-1904. https://doi.org/10.1007/s00202-024-02618-y

[7] Zeng, L. & Chiang, H.-D. (2024). Online and look-ahead determination of the renewable admissible region for managing the uncertainty of renewables: Theory and some applications. *IEEE Transactions on Power Systems*, *39*(4), 5609-5619. https://doi.org/10.1109/TPWRS.2023.3344722

[8] Yang, X. H. et al. (2023). An optimised scheduling strategy combining robust optimisation and rolling optimisation to address the uncertainty of RES-CCHP microgrids. *Renewable Energy*, *211*, 307-325. https://doi.org/10.1016/j.renene.2023.04.103

[9] Wen, L., Zhou, K., Feng, W., & Yang, S. (2024). Demand side management in smart grid: A dynamic-price-based demand response model. *IEEE Transactions on Engineering Management*, *71*, 1439-1451. https://doi.org/10.1109/TEM.2022.3158390

[10] Muratori, M. & Rizzoni, G. (2016). Residential demand response: Dynamic energy management and time-varying

electricity pricing. *IEEE Transactions on Power Systems*, *31*(2), 1108-1117. https://doi.org/10.1109/TPWRS.2015.2414880

[11] Qu, K., Chen, Y., Xie, S., Zheng, X., & Zhu, J. (2024). Segmented distributionally robust optimisation for real-time power dispatch with wind uncertainty. *IEEE Transactions on Power Systems*, *39*(2), 2970-2983. https://doi.org/10.1109/TPWRS.2023.3303313

[12] Stratigakos, A., Andrianesis, P., Michiorri, A., & Kariniotakis, G. (2024). Towards resilient energy forecasting: A robust optimization approach. *IEEE Transactions on Smart Grid*, *15*(1), 874-885. https://doi.org/10.1109/TSG.2023.3272379

[13] Zhang, J. et al. (2025). Optimal planning for electricity-gas-hydrogen integrated energy systems considering intertemporal long-term hydrogen storage and multiple uncertainties. *IEEE Transactions on Power Systems. Advance online publication*, *40*(6), 4660-4674. https://doi.org/10.1109/TPWRS.2025.3577703

[14] Wang, K. et al. (2023). A coordinated reconfiguration strategy for multi-stage resilience enhancement in integrated power distribution and heating networks. *IEEE Transactions on Smart Grid*, *14*(4), 2709-2722. https://doi.org/10.1109/TSG.2022.3231590

[15] Weng, Y., Luo, S., Cui, Q., Trask, R., & Wang, H. (2023). Evaluate DC meter adoption for house-level storage devices. *IEEE Transactions on Smart Grid*, *14*(1), 464-475. https://doi.org/10.1109/TSG.2022.3188506

[16] Sharma, A. & Sharma, S. (2024). Demand response assisted energy and reserve procurement in renewable integrated dynamic energy market. *Electric Power Systems Research*, *236*, 110932. https://doi.org/10.1016/j.epsr.2024.110932

[17] Alirezaei, R., Dashti, R., & Mirhosseini, M. (2025). Analysis of energy supply scenarios using grid-connected hybrid systems: Investigating time-of-use demand response strategy for improving operational performance. *Energy*, *318*, 134596. https://doi.org/10.1016/j.energy.2025.134596

[18] Ghanuni, A., Sharifi, R., & Feshki Farahani, H. (2023). A risk-based multi-objective energy scheduling and bidding strategy for a technical virtual power plant. *Electric Power Systems Research*, *220*, 109344. https://doi.org/10.1016/j.epsr.2023.109344

[19] Zhou, A., Khodayar, M. E., & Wang, J. (2024). Distributionally robust optimal scheduling with heterogeneous uncertainty information: A framework for hydrogen systems. *IEEE Transactions on Sustainable Energy*, *15*(3), 1933-1945. https://doi.org/10.1109/TSTE.2024.3388388

[20] Zare Oskouei, M., Mehrjerdi, H., & Palensky, P. (2024). Risk-constrained bidding and offering strategy for sector-coupled electricity-hydrogen systems in corporating accessibility level of mobility sector. *Journal of Cleaner Production*, *451*, 142031. https://doi.org/10.1016/j.jclepro.2024.142031

[21] Azimi, M., Salami, A., Javadi, M. S., & Catalão, J. P. S. (2024). Optimal and distributed energy management in interconnected energy hubs. *Applied Energy*, *365*, 123282. https://doi.org/10.1016/j.apenergy.2024.123282

Contact information:

Haoyu MAO
College of Information Engineering, Nanchang University,
Nanchang 330031, Jiangxi, China
E-mail: 5811123074@email.ncu.edu.cn